TU Delft

Delft University of Technology

Document Version
Final published version

Licence
CC BY

Citation (APA)
Pfanner, E., Lin, Y. C., & Tang, Y. (2026). Linking Oxide Scale Evolution to Thermal Shock Failure in Zirconium Carbide. *International Journal of Applied Ceramic Technology*, *23*(5), Article e70284. https://doi.org/10.1111/ijac.70284

Important note
To cite this publication, please use the final published version (if applicable).
Please check the document version above.

Copyright
In case the licence states “Dutch Copyright Act (Article 25fa)”, this publication was made available Green Open Access via the TU Delft Institutional Repository pursuant to Dutch Copyright Act (Article 25fa, the Taverne amendment). This provision does not affect copyright ownership.
Unless copyright is transferred by contract or statute, it remains with the copyright holder.

Sharing and reuse
Other than for strictly personal use, it is not permitted to download, forward or distribute the text or part of it, without the consent of the author(s) and/or copyright holder(s), unless the work is under an open content license such as Creative Commons.

Takedown policy
Please contact us and provide details if you believe this document breaches copyrights.
We will remove access to the work immediately and investigate your claim.

This work is downloaded from Delft University of Technology.

Check for updates

International Journal of Applied Ceramic Technology

RESEARCH ARTICLE OPEN ACCESS

Linking Oxide Scale Evolution to Thermal Shock Failure in Zirconium Carbide

Eden Pfanner | Yun-Ching Lin | Yinglu Tang

Department of Aerospace Structures and Materials, Faculty of Aerospace Engineering, Delft University of Technology, Delft, The Netherlands

Correspondence: Eden Pfanner (edenpfanner@gmail.com) | Yinglu Tang (y.tang-5@tudelft.nl)

Received: 16 April 2026 | **Revised:** 19 August 2026 | **Accepted:** 16 September 2026

Keywords: thermal cycling | thermal shock | ultra-high-temperature ceramics | zirconium carbide

ABSTRACT

Zirconium carbide (ZrC) is an ultra-high-temperature ceramic valued for its excellent thermomechanical properties, yet its vulnerability to oxidation and its thermal shock behavior upon oxidation remain insufficiently understood. This study examines how prior oxidation history, defined by cyclic exposure temperature and duration, affects the thermal shock response of monolithic ZrC. Near-stoichiometric specimens were oxidized in atmospheric air across a temperature range of 600°C–800°C, then water-quenched from those temperatures. Increasing oxidation severity produced thicker oxide scales, higher monoclinic ZrO_2 content, and greater crack density. A transition to failure-prone behavior occurred between 700°C and 800°C, when monoclinic ZrO_2 and crack density both exceeded approximately 10%, leading to critical degradation. Given the oxidation parameters explored, the temperature threshold for thermal shock occurrence was identified as 700°C–800°C. The combined oxidation–quench approach establishes oxidation-dependent thresholds for thermal shock resistance and provides a framework for evaluating the stability of oxidized structures in harsh thermal environments.

1 | Introduction

Zirconium carbide (ZrC) is an ultra-high-temperature ceramic (UHTC) valued for its desirable thermomechanical properties [1]. These properties make it a strong candidate for use in extreme thermal environments, where mechanical strength and efficient heat dissipation are critical. Space represents a key application environment for UHTCs, particularly in spacecraft thermal protection systems that must withstand severe thermal loads during orbit, atmospheric re-entry, and other high-temperature transients. Under these conditions, large thermal gradients can generate significant internal stresses, leading to cracking or even catastrophic failure [2]. Therefore, despite the favorable thermomechanical properties of UHTCs, the susceptibility of ZrC to oxidative degradation during thermal cycling and subsequent thermal shock remains a major limitation to its long-term performance and structural reliability [3].

Oxidation of ZrC initiates at elevated temperatures, typically above 500°C, and becomes progressively more severe at higher temperatures [4]. The oxidation process is best described by the formation of zirconia (ZrO_2) and carbon oxides (CO and CO_2) through the following primary reactions:

$$ZrC + 2\,O_2 \rightarrow ZrO_2 + CO_2$$

$$2\,ZrC + 3\,O_2 \rightarrow 2\,ZrO_2 + 2\,CO$$

These reactions are both thermodynamically favorable and experimentally validated across oxygen partial pressures ranging from approximately 0.01 to 101 kPa and temperatures from

This is an open access article under the terms of the Creative Commons Attribution License, which permits use, distribution and reproduction in any medium, provided the original work is properly cited.
© 2026 The Author(s). *International Journal of Applied Ceramic Technology* published by Wiley Periodicals LLC on behalf of American Ceramics Society.

approximately 500°C to above 1500°C [4–6]. During oxidation, volatile byproducts (CO and CO_2) escape from the surface, often resulting in porosity, internal cracking, and morphological instability within the growing oxide scale.

In addition to direct ZrO_2 formation, several studies report an intermediate carbon-containing layer at the ZrC/ZrO_2 interface. Typically consisting of free or amorphous carbon embedded within the growing oxide, this layer forms as oxygen diffuses into the carbide lattice while displacing carbon, which subsequently escapes in the form of CO/CO_2 [3, 5]. The resultant combined effects of porosity, cracking, and the intermediate layer compromise the mechanical integrity of the oxide scale, leading to delamination, microcracking, spallation, and the progressive degradation of ZrC's thermomechanical properties, including thermal shock resistance [3].

Beyond these structural defects, the as-formed ZrO_2 also undergoes polymorphic phase transformations that further reduce its thermal shock resistance. Zirconia, the principal oxidation product of ZrC, can exist in three crystallographic polymorphs: cubic (*c*), tetragonal (*t*), and monoclinic (*m*), each with distinct thermodynamic stabilities, microstructures, and mechanical behaviors. Tetragonal and cubic phases are typically stable at high temperatures, while monoclinic ZrO_2 is stable at lower temperatures (<1170°C) [3, 7, 8]. However, temperature is not the only determining factor; the actual phase distribution during oxidation is also strongly influenced by grain size and growth constraints. In thin or fine-grained oxide layers, tetragonal ZrO_2 can be stabilized by surface energy and compressive strain even at lower temperatures, whereas tensile stresses associated with grain coarsening or cooling promote transformation to monoclinic ZrO_2, making the oxidation behavior highly microstructure-dependent [9].

With grain growth, metastable *t*/*c*-ZrO_2 often transforms to *m*-ZrO_2, a process that is accompanied by a 3%–5% volume expansion [7]. This transformation produces complex stress states, as the expanding grains exert compressive forces on the surrounding oxide. Depending on the thermal history, these stresses may exceed the fracture toughness of the oxide, initiating microcracks and contributing to oxide failure. Additionally, the coefficient of thermal expansion (CTE) mismatch between ZrC and ZrO_2 phases further amplifies stress generation. At room temperature, ZrC has a CTE of roughly 4×10^{-6} K^{-1}, while *t*-ZrO_2 and *c*-ZrO_2 have CTEs ranging from 10–11.5 $\times 10^{-6}$ K^{-1} [1, 10, 11]. *m*-ZrO_2, although lower on average (~2–9 $\times 10^{-6}$ K^{-1}), exhibits highly anisotropic behavior due to its low-symmetry monoclinic lattice, where expansion varies strongly along different crystallographic axes [10]. These mismatches create interfacial stress concentrations that intensify as the oxide scale grows and evolves during thermal exposure [12].

With the development of these residual stresses, the thermal shock response of the oxide–substrate system becomes increasingly dependent on its thermomechanical properties. The thermal shock response of ceramics is governed by the combined effects of elastic modulus, fracture resistance, CTE, and thermal conductivity, which together control the magnitude of thermally induced stresses and the material's resistance to crack initiation and propagation during rapid temperature changes [13, 14]. Consequently, the zirconia oxide scale is expected to be more susceptible to cracking and delamination than the underlying ZrC substrate because it experiences transformation-induced strain in addition to thermal expansion mismatch. As oxidation progresses and the oxide develops, these stresses are expected to become increasingly concentrated within the scale and near the oxide–substrate interface, promoting crack initiation, interfacial degradation, and eventual spallation.

Pristine ZrC exhibits moderate thermal shock resistance, with water-quench tests reporting a critical temperature difference of approximately 233°C and fracture toughness in the 1–4 $MPa \cdot m^{1/2}$ range [15]. Its relatively high thermal conductivity (~30–37 W/m·K from 150°C to 1000°C) helps distribute heat and reduce stress gradients. Thermal shock further interacts with existing oxide layers: during rapid cooling, such as water quenching, steep thermal gradients through the oxide scale and substrate generate high transient stresses [16]. Oxide scales formed during prior oxidation may therefore be particularly susceptible to cracking or delamination under subsequent shock loading [17]. Zhang et al., for example, studied $MoSi_2$–ZrB_2–SiC composites and observed that oxidative pretreatment reduced flexural strength under subsequent water-quench thermal shock [18]. While this system differs from ZrC, their results highlight a broader principle: oxidation prior to shock exposure diminishes mechanical resilience in UHTCs. Several studies have since examined thermal shock behavior in UHTCs, with ZrC receiving increasing attention in recent years.

Despite the previous efforts in linking prior oxidation to thermal shock behavior, the extent and nature of these effects remain unclear. This uncertainty arises because thermal shock response is strongly influenced by oxide-scale characteristics, including thickness, phase composition, residual stress, and crack density, all of which are governed by the oxidation conditions under which the scale develops. Most prior work has focused on long-duration isothermal oxidation [9], where oxide scales grow steadily under constant conditions [3, 8]. Recent studies have continued this approach [19, 20]. For example, Konnik et al. demonstrated that oxide morphology and phase composition varied noticeably with temperature, with *t*-ZrO_2 forming at higher temperatures (>1400°C) to produce compact, adherent scales, while lower-temperature oxidation (<1200°C) led to porous, unstable monoclinic oxides prone to disintegration [19]. Valuable as it is, this approach overlooks the practical relevance of thermal cycling in operational environments, where materials experience repeated heating and cooling sequences.

Consequently, the influence of thermal cycling on oxide-scale development warrants particular attention. Thermal cycling introduces repeated expansion and contraction events, which affect oxide nucleation, growth rate, and microstructural evolution differently from isothermal conditions. Thermal cycling has been studied in other UHTCs, such as HfC by Courtright et al. and ZrB_2–SiC ceramics by Levine et al.; these studies show that cyclic oxidation can modify oxide-scale growth kinetics, promote cracking and spallation, and increase damage accumulation relative to equivalent isothermal exposures [20, 21]. However, these findings cannot be directly extended to ZrC due to differences in oxidation mechanisms, phase behavior, and microstructural evolution [21]. In ZrC, the role of thermal cycling in governing oxide evolution and subsequent damage response has not been

17447402, 2026, 5, Downloaded from https://ceramics.onlinelibrary.wiley.com/doi/10.1111/ijac.70284 by Technical University Delft, Wiley Online Library on [01/10/2026]. See the Terms and Conditions (https://onlinelibrary.wiley.com/terms-and-conditions) on Wiley Online Library for rules of use; OA articles are governed by the applicable Creative Commons License

systematically studied. To date, no published studies have systematically investigated cyclic oxidation behavior in monolithic ZrC, making this an open area of research with significant implications for oxidation kinetics and post-oxidation mechanical stability.

This study investigates how cyclic oxidation temperature and duration affect the thermal shock resistance of oxide scales on ZrC, focusing on the under-explored regimen of intermediate temperatures (600°C–800°C) and short cycling durations. These conditions preserve the oxide scale, simplify post-shock analysis, and still yield relevant oxidation products. By subjecting monolithic ZrC specimens to cyclic oxidation at temperatures ranging from 600°C to 800°C, followed by rapid thermal shock via water quenching, this work aims to quantify how oxidation severity affects the mechanical stability of the oxide layer. Through analysis with x-ray diffraction (XRD), Raman spectroscopy, and scanning electron microscopy (SEM), degradation thresholds are identified in terms of monoclinic phase content and crack density. Thus, this study provides insight into the failure mechanisms of oxide layers under coupled cyclic oxidative and thermal shock loading and helps define practical limits for ZrC use in extreme thermal environments.

2 | Materials and Methods

2.1 | Material and Sample Preparation

The material used in this study consists of monolithic ZrC specimens fabricated via SPS with an HP D 25 SD furnace (FCT Systeme GmbH, Germany) in a graphite die under vacuum. The specimen fabrication procedure is summarized here; a complete description of the materials processing is provided in a previous publication [22]. The ZrC powder was sourced from Goodfellow (purity: 99.5%, particle size ≤45 μm, UK) and was sintered using a two-step heating schedule. Two-step sintering was carried out at 1500°C for 120 s, followed by 2000°C for 600 s under 80 MPa uniaxial pressure with a heating rate of 3.3°C/s. The sintered sample was cooled to room temperature with a cooling rate of 0.4°C/s, and the remaining graphite on the surface of the ZrC ceramic disk was removed with a grinder-polisher (MetaServ 250, Buehler, USA).

SPS was selected because it enables the fabrication of highly dense ZrC with reduced porosity, which is critical for reproducible oxidation and thermal shock testing. Prior to testing, all specimens were cleaned with ethanol to remove surface debris, and no coatings or surface treatments were applied. This process produced ceramics with an average density of 6.64 ± 0.01 g/cm^3 [22] (relative to the theoretical density of 6.73 g/cm^3 for ZrC [1]). Despite some minor variations in size and shape, which result from the limitations of the available material, all specimens were geometrically similar (with masses ranging from 184.9 to 315.1 mg) to ensure consistent orientation and placement during testing.

2.2 | Thermal Cycle-Induced Oxidation

Oxidation was performed through a series of controlled thermal cycles in air at elevated temperatures using a thermo-mechanical analyzer (TMA) (PerkinElmer, USA). The TMA measurements were performed in ambient laboratory air at atmospheric pressure, without active control of gas composition or moisture level. Therefore, the atmosphere cannot be classified as dry air, and no specific purity level is defined. The thermal cycling schedule in Table 1 was designed accordingly, with a generalization of the profiles displayed in Figure 1.

TABLE 1 | Experimental matrix for thermal cycling.

Sample	Low temp.	Dwell time (min)	High temp.	Dwell time (min)
600-3	−70°C	3	600°C	3
600-40	−70°C	10	600°C	40
700-3	−70°C	3	700°C	3
700-5	−70°C	5	700°C	5
800-3	−70°C	3	800°C	3
800-5	−70°C	5	800°C	5

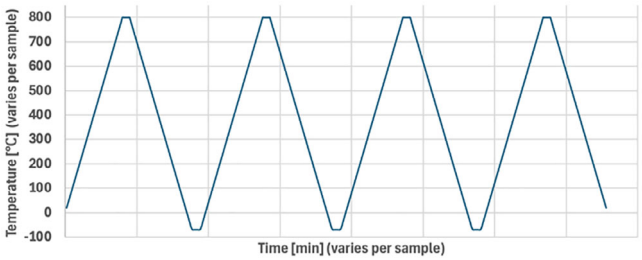


FIGURE 1 | Example of heating profile during thermal cycling.

Each sample underwent four complete thermal cycles between its designated low and high temperatures. Four cycles were selected to promote measurable oxide growth while limiting excessive oxide loss through spallation, allowing the influence of oxidation severity on subsequent thermal shock behavior to be isolated. A consistent heating and cooling rate of 20°C/min was used to minimize thermal gradients. The temperature range for cycling was 600°C–800°C to achieve a variety of oxidation states, while the minimum temperature remained at −70°C to introduce repeated thermal contraction (within the operating limits of the TMA). This ramp rate and temperature window were selected based on previous studies, which indicate that these conditions capture early-stage oxidation in ZrC without inducing severe spallation [3, 22]. The dwell periods at the peak temperature were selected to ensure thermal equilibration of the small specimens while providing different oxidation exposures at each temperature.

2.3 | Thermal Shock Testing

After cyclic oxidation, each sample was reheated under argon in a Lenton PTF 16/75/610 tube furnace (Lenton, UK) to its respective peak oxidation temperature (600°C, 700°C, or 800°C). The inert atmosphere prevents additional oxidation during reheating, preserving the oxide layer formed during thermal cycling. Following a 10-min hold to ensure thermal equilibration, samples were immediately quenched in room-temperature water (20°C),

17447402, 2026, 5, Downloaded from https://ceramics.onlinelibrary.wiley.com/doi/10.1111/ijac.70284 by Technical University Delft, Wiley Online Library on [01/10/2026]. See the Terms and Conditions (https://onlinelibrary.wiley.com/terms-and-conditions) on Wiley Online Library for rules of use; OA articles are governed by the applicable Creative Commons License

generating thermal gradients of approximately 580°C, 680°C, and 780°C for the 600°C, 700°C, and 800°C samples, respectively. Samples were fully submerged during quenching, and identical quenching procedures were used for all specimens to ensure consistent thermal shock conditions. These abrupt temperature drops produce internal stresses that simulate thermal shock. Observing the resulting damage (including oxide spallation, crack formation, and delamination) provides insight into failure mechanisms associated with prior oxidation history.

2.4 | Phase Composition and Microstructural Characterization

Following each thermal cycle and shock, the specimens were analyzed to monitor oxide scale progression and to characterize its degradation. XRD was used to identify surface phases upon oxidation using a Rigaku Miniflex 600 diffractometer (Rigaku, Japan) operating at 40 kV and 15 mA. Diffraction patterns were collected directly from the oxidized specimen surfaces over a 2θ range of 20°–85°, with a step size of 0.02°, and a scan speed of 1.2°/min. Due to peak broadening, tetragonal and cubic zirconia phases were grouped together (t/c-ZrO_2) [3]. Rietveld refinement was performed in Profex, which iteratively fits simulated diffraction patterns to the experimental XRD data to quantify phase fractions. Reference structures were taken from the Materials Project database (mp-2795 for ZrC, mp-2858 for m-ZrO_2, mp-2574 for t-ZrO_2, and mp-1565 for c-ZrO_2). However, the results primarily represent the thin oxide surface layer rather than the bulk material.

Raman spectroscopy was used to complement XRD by detecting zirconia polymorphs and carbonaceous residues with higher surface sensitivity [9]. Spectra were collected with a Renishaw inVia confocal Raman microscope (Renishaw, UK) using a 532 nm excitation source, over 100–2000 cm^{-1}, with a 10-s integration time and 10 accumulations per point. The selected spectral range captures both zirconia lattice modes and carbon-related features, enabling identification of oxide phases and residual carbonaceous species. Particular attention was given to the characteristic m-ZrO_2 peaks near 177–190, 223, 307, 336, 476, 615, and 640 cm^{-1}, as well as the t-ZrO_2 peaks near 148, 267, 320, 462, and 605 cm^{-1} [23]. Due to overlap between tetragonal and cubic zirconia bands and the weak Raman response of c-ZrO_2, ambiguous features were interpreted collectively as t/c-ZrO_2.

In addition to phase identification, qualitative changes in Raman peak position, width, and shape were used as indicators of residual stress, structural disorder, and phase stability within the oxide scale [24]. Residual stress was estimated from Raman peak shifts using a phase-specific piezospectroscopic approach. Characteristic Raman bands were isolated within predefined spectral windows, locally baseline-corrected, and fitted with single or multiple Gaussian profiles, as appropriate, by minimizing the sum of squared residuals between the measured and fitted intensities to determine their center positions. Residual stress was then calculated according to $\sigma = \frac{\nu_0}{\Pi}$ where ν is the fitted peak position, ν_0 is the stress-free reference position, and Π is the mode-specific piezospectroscopic coefficient [24, 25]. To evaluate the effect of thermal shock, the change in residual stress was also calculated as

$$\Delta\sigma = \nu_{\text{post-shock}} - \nu_{\text{pre-shock}}$$

allowing stress redistribution before and after quenching to be quantified. The low-frequency monoclinic bands near 178 and 190 cm^{-1} were selected because they were well-resolved, phase-specific peaks with established piezospectroscopic calibrations and have been shown to be particularly sensitive to residual stress while being minimally affected by grain size and oxygen non-stoichiometry [25, 26]. For t/c-ZrO_2, the 145 cm^{-1} band was selected because it possesses experimentally calibrated piezospectroscopic coefficients and exhibits higher reliability for stress analysis than the higher wavenumber tetragonal modes, where overlap with m-ZrO_2 complicates interpretation in mixed-phase oxide scales [25]. Because the calibration coefficients were obtained from bulk zirconia reported in the literature rather than thermally grown oxide scales on ZrC, the calculated values are interpreted as Raman-derived local residual stress estimates that enable comparison between oxidation conditions and before and after thermal shock rather than absolute macroscopic stresses within the oxide. Peak broadening was associated with disorder, fine grain size, and phase overlap, while stress-induced peak shifts provided insight into the evolution of oxidation-induced strain and its relationship to cracking and oxide degradation.

SEM with a JSM-7500F microscope (JEOL, Japan) was employed to directly observe the microstructural features of the oxide scales, including surface and cross-sectional morphology, cracking, and delamination. Surface SEM images were obtained directly from the oxidized specimens without additional preparation, whereas cross-sectional analysis required the specimens to be sectioned, mounted, and polished prior to imaging. While SEM cannot differentiate zirconia polymorphs, it reveals the physical manifestations of degradation, bridging the link between phase evolution and mechanical damage.

Crack densities were quantified from SEM images using ImageJ by thresholding the images to isolate visible cracks and calculating the cumulative crack area as a percentage of the total analyzed image area. For each sample, three images of similar magnification and field of view were analyzed for both surface and cross-sectional regions, and the average value was reported. Crack density was defined as the percentage of the analyzed area occupied by cracks, providing a measure of the extent of microstructural damage rather than the number of individual cracks. This area-based metric was selected because crack propagation and coalescence during oxidation can reduce the apparent crack count despite increasing damage severity. Consequently, crack density reflects the degree of oxide fragmentation and loss of structural integrity within the analyzed region.

Oxidation progression was also evaluated through measurements of mass change and oxide scale thickness. Mass change was determined by comparing specimen masses between thermal cycles and after thermal shock, providing an indication of oxygen uptake during oxidation. Oxide scale thicknesses were measured from SEM cross-sectional images using the SEM ruler tool. Thickness was defined as the perpendicular distance from the oxide surface to the oxide–substrate interface for the outer oxide layer and, where present, to the boundaries of the intermediate layer. Three measurements were collected along each cross-section to account for non-uniform oxide growth, and the

17447402, 2026, 5, Downloaded from https://ceramics.onlinelibrary.wiley.com/doi/10.1111/ijac.70284 by Technical University Delft, Wiley Online Library on [01/10/2026]. See the Terms and Conditions (https://onlinelibrary.wiley.com/terms-and-conditions) on Wiley Online Library for rules of use; OA articles are governed by the applicable Creative Commons License

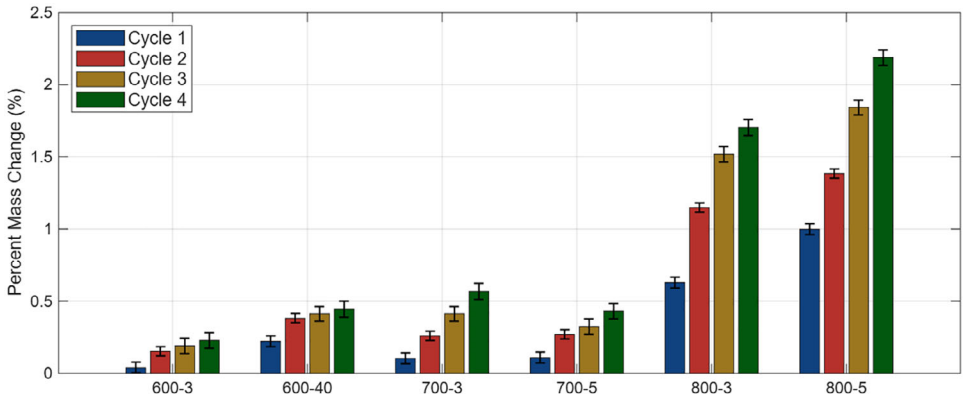


FIGURE 2 | Changes in mass throughout four thermal cycles with respect to initial mass.

average thickness was reported. Together, these complementary techniques enabled a correlative analysis of oxidation-driven degradation, linking phase evolution, stress development, and microstructural damage in ZrC.

3 | Results and Discussion

3.1 | Oxide Scale Development Throughout Thermal Cycling

To begin the study, samples were oxidized through controlled thermal cycling, resulting in measurable changes in both oxide scale thickness and phase composition. Each sample underwent four complete thermal cycles between 600°C and 800°C, promoting progressive oxide growth under controlled transient conditions without triggering full-scale spallation, ensuring the oxide scale remained analyzable after thermal shock. Previous work on ZrB_2–SiC–C composites has shown that repeated short oxidation cycles at sufficiently high temperatures produce progressive surface roughening, oxide non-uniformity, and steady weight gain, with changes becoming visible after five cycles and severe by 10 [21]. Similarly, four cycles were selected for our ZrC samples to initiate measurable surface evolution while avoiding excessive cracking or scale loss. Upon cycling, XRD and Raman spectroscopy analyses revealed a clear evolution in oxide structure with increasing peak cycle temperature.

The first indication of oxide scale formation was an increase in mass among each sample. Oxidation is characterized by an uptake of oxygen, producing zirconia and adding mass to the sample; the rate at which this process occurs gives insight into the state of oxidation that is occurring. The changes in mass in the samples are visualized in Figure 2.

Samples oxidized at 800°C exhibited the greatest mass gains, indicating accelerated oxide growth and oxygen uptake at higher temperatures. In contrast, samples oxidized at 600°C and 700°C showed substantially smaller mass increases, reflecting slower oxidation kinetics and thinner oxide-scale development. These results demonstrate that oxidation behavior is strongly temperature dependent, with higher temperatures promoting more extensive oxide growth and mass gain. Additionally, Table 2 quantifies oxide scale thickness and highlights the emergence of a two-layer structure at higher temperatures.

TABLE 2 | Oxide scale thickness after thermal cycling.

	600–3	600-40	700-3	700-5	800-3	800-5
Outer layer [μm ± 0.06 μm]	3.4	3.9	18.8	29.6	143.8	149.0
Intermediate layer [μm ± 0.06 μm]	0	2.3	1.3	3.4	4.2	3.4

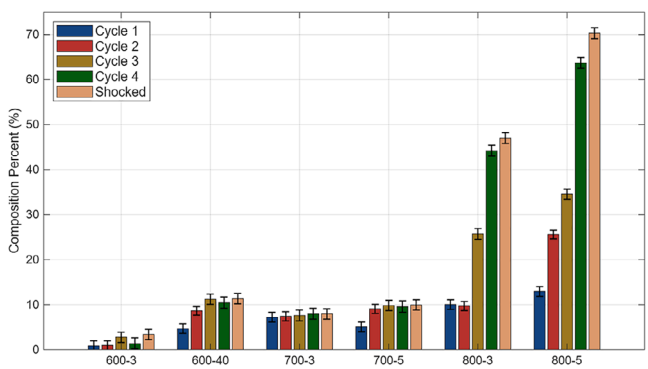


FIGURE 3 | m-ZrO_2 surface concentrations after each thermal cycle and shock.

The outer oxide layer increased in thickness with both oxidation time and temperature. An intermediate layer, present in samples beyond 600-3, likely represents a compact transition zone between the porous oxide and the underlying substrate. Higher oxidation temperatures and longer exposure durations produced thicker, more developed oxide scales, reflecting the increasing severity of oxidation under these conditions.

3.2 | Oxidation-Driven Surface Evolution Prior to Thermal Shock

At lower oxidation temperatures, XRD patterns and Rietveld refinement (processed into Figures 3–5) showed the presence

17447402, 2026, 5, Downloaded from https://ceramics.onlinelibrary.wiley.com/doi/10.1111/ijac.70284 by Technical University Delft, Wiley Online Library on [01/10/2026]. See the Terms and Conditions (https://onlinelibrary.wiley.com/terms-and-conditions) on Wiley Online Library for rules of use; OA articles are governed by the applicable Creative Commons License

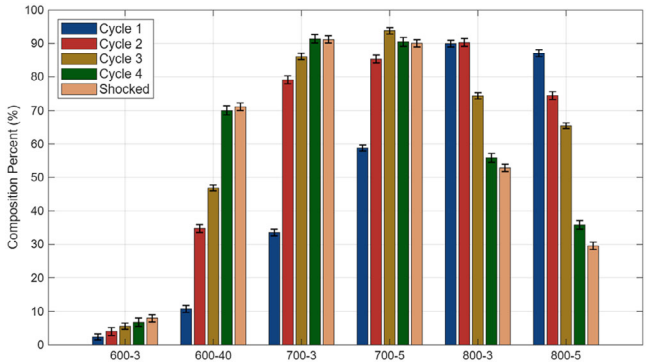


FIGURE 4 | t/c-ZrO_2 surface concentrations after each thermal cycle and shock.

of metastable t/c-ZrO_2, consistent with the rapid formation of nanocrystalline structures during early oxidation [3, 7, 8]. However, as temperature and duration increased, these phases progressively diminished while the characteristic monoclinic peaks became increasingly dominant [27, 28]. This progression from t/c-ZrO_2 to m-ZrO_2 reflects the destabilization of metastable phases in favor of the thermodynamically stable monoclinic form, confirming that the oxide layer evolves continuously during cycling rather than remaining static. Consequently, the samples span a controlled spectrum of oxide surface states, from partially transformed metastable scales to nearly fully monoclinic surfaces, which provide a systematic basis for examining degradation mechanisms under subsequent thermal shock.

The measured phase fractions also provide insight into stress evolution within the oxide scale. Samples retaining larger fractions of t/c-ZrO_2 likely contained a greater proportion of oxide stabilized by mechanical constraint or fine grain size, indicating that the developing scale remained under conditions that suppressed complete transformation to the monoclinic phase. As oxidation temperature and duration increased, the progressive rise in m-ZrO_2 suggests a loss of this stabilization through grain growth and continued oxide development. This phase evolution has important mechanical implications because the $t/c \rightarrow m$ transformation is accompanied by a 3%–5% volume expansion. Consequently, increasing monoclinic content likely reflects not only advancing oxidation but also the accumulation and redistribution of transformation-induced stresses within the oxide scale. These stresses can be partially relieved through cracking, delamination, and local stress relaxation.

Complementary Raman spectra (Figures 6 and 7) reinforced the phase evolution observed by XRD. At lower oxidation temperatures, the spectra retained features associated with metastable t/c-ZrO_2, whereas higher temperature cycling produced increasingly dominant monoclinic signatures, indicating progressive transformation toward the thermodynamically stable phase [23]. In parallel, a broad feature near 1000 cm^{-1} grew more prominent in higher temperature samples. This band, often linked to defect-induced modes or second order scattering in zirconia, indicates stress buildup within the oxide layer [24, 29]. Its intensification suggests that thermal cycling not only drove phase transformation toward monoclinic zirconia, but also promoted residual stress accumulation, likely due to volumetric expansion mismatches and grain coarsening during oxidation [9]. These Raman results expand upon the XRD findings by showing that zirconia phase evolution and stress redistribution scale with oxidation temperature and duration, producing progressively more complex and mechanically vulnerable oxide structures. Quantitative changes in Raman-derived residual stress due to thermal shock are examined in Section 3.3 using peak-shift analysis of selected zirconia Raman modes.

These trends were also evident in SEM analysis, which showed that crack formation intensified with increasing oxidation severity, as quantified in Table 3. At lower oxidation temperatures, both surface and internal crack densities remained relatively low, with the oxide layers appearing thin and largely conformal to the underlying ZrC structure, consistent with compliant scales that mainly accommodate strain through surface cracking. However, at higher oxidation temperatures, crack densities rose significantly (as pictured in Figure 8), particularly within the cross-sections of the 700- and 800-series samples. Crack morphology evolved from isolated surface cracks to dense, interconnected crack networks, with through-thickness cracking, porous and fragmented regions, and local delamination becoming increasingly prevalent. This shift reflects the transition to a brittle failure regimen, where the stored strain energy is released through deep fracture propagation.

Figure 8 shows that cracking was confined to the oxide scale, with no observable cracks in the underlying ZrC substrate. In the less severely oxidized samples, cracks were concentrated near the oxide surface, whereas increasing oxidation severity produced more extensive cracking throughout the scale and near the oxide–substrate interface. This progression is consistent with the accumulation of stresses arising from thermal expansion mismatch and $t/c \rightarrow m$ transformation strain during oxide growth. Consequently, damage became increasingly concentrated within the oxide and near the interface, while the ZrC substrate remained structurally intact.

The moderate 20°C/min heating and cooling rate was deliberately chosen to promote gradual oxide growth rather than severe thermal shock stresses. Instead, repeated cycles promoted gradual oxide growth and the accumulation of oxidation-induced stresses arising from thermal expansion mismatch, phase evolution, and cyclic expansion–contraction. As oxidation severity increased, these stresses progressively degraded the oxide scale, driving crack initiation, propagation, and eventual loss of structural integrity.

These SEM observations indicate progressive oxidation-induced degradation, with internal crack density ranging from 2.00% ± 0.5% in samples with relatively thin oxide scales (3.96 ± 0.1 μm in 600-40) to 20.47% ± 2.9% in samples with thicker scales (149 ± 0.1 μm in 800-3). Moreover, oxide thickness alone did not consistently predict damage severity; for example, although 800-5 exhibited the thickest scale, its crack density was lower than that of 800-3 (as evidenced by Table 3), which is likely related to greater $t/c \rightarrow m$ phase transformation and the resulting residual stress development (Figures 3–7). This layered oxide architecture, characteristic of prolonged high-temperature oxidation, suggests that damage evolution is governed not only by oxide growth

17447402, 2026, 5, Downloaded from https://ceramics.onlinelibrary.wiley.com/doi/10.1111/ijac.70284 by Technical University Delft, Wiley Online Library on [01/10/2026]. See the Terms and Conditions (https://onlinelibrary.wiley.com/terms-and-conditions) on Wiley Online Library for rules of use; OA articles are governed by the applicable Creative Commons License

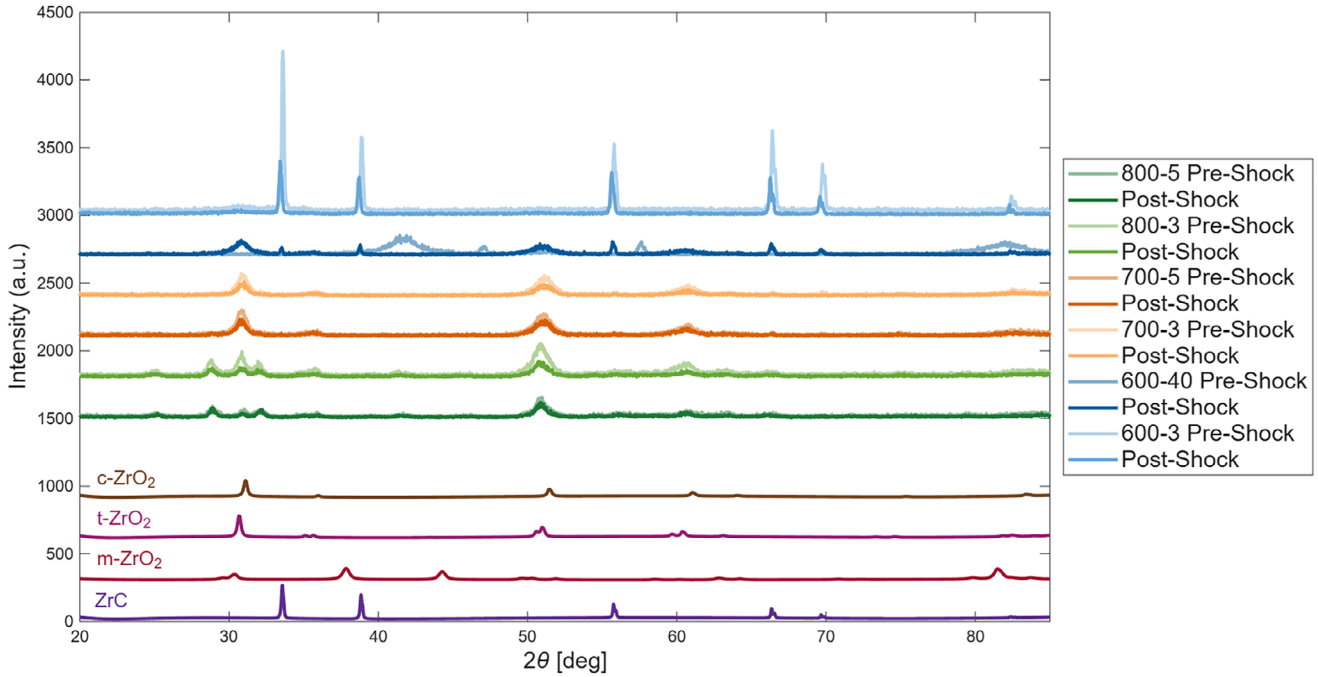


FIGURE 5 | XRD diffraction patterns before and after thermal shock.

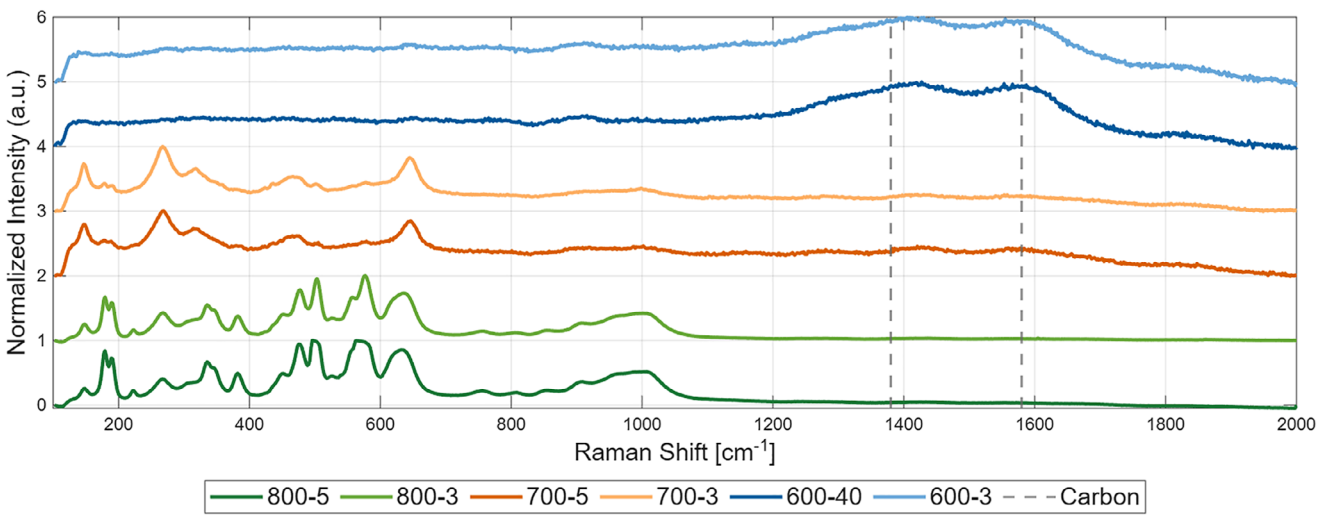


FIGURE 6 | Raman spectra of all samples after four thermal cycles from 100 to 2000 cm^{-1}.

TABLE 3 | Crack density (surface and internal) of samples after thermal cycling.

Image	600-3	600-40	700-3	700-5	800-3	800-5
Surface	2.25% ± 0.5%	5.97% ± 1.7%	6.49% ± 1.7%	13.60% ± 1.7%	13.97% ± 1.7%	13.53% ± 1.7%
Cross-section	0.43% ± 0.5%	2.00% ± 0.5%	6.75% ± 1.7%	8.48% ± 1.7%	20.47% ± 2.9%	17.75% ± 2.9%

but also by factors such as phase composition and residual stress development. Together, these findings demonstrate that oxidation severity governs the evolution of phase composition, residual stress, and microstructural damage, establishing the initial condition that controls the subsequent thermal shock response.

3.3 | Microstructural Damage Evolution After Shock

Upon thermal shock of the oxidized samples, refined XRD data (Figures 3 and 4) revealed a modest but consistent increase in *m*-ZrO_2 content across all samples, indicating that residual *t*/*c*-

17447402, 2026, 5, Downloaded from https://ceramics.onlinelibrary.wiley.com/doi/10.1111/ijac.70284 by Technical University Delft, Wiley Online Library on [01/10/2026]. See the Terms and Conditions (https://onlinelibrary.wiley.com/terms-and-conditions) on Wiley Online Library for rules of use; OA articles are governed by the applicable Creative Commons License

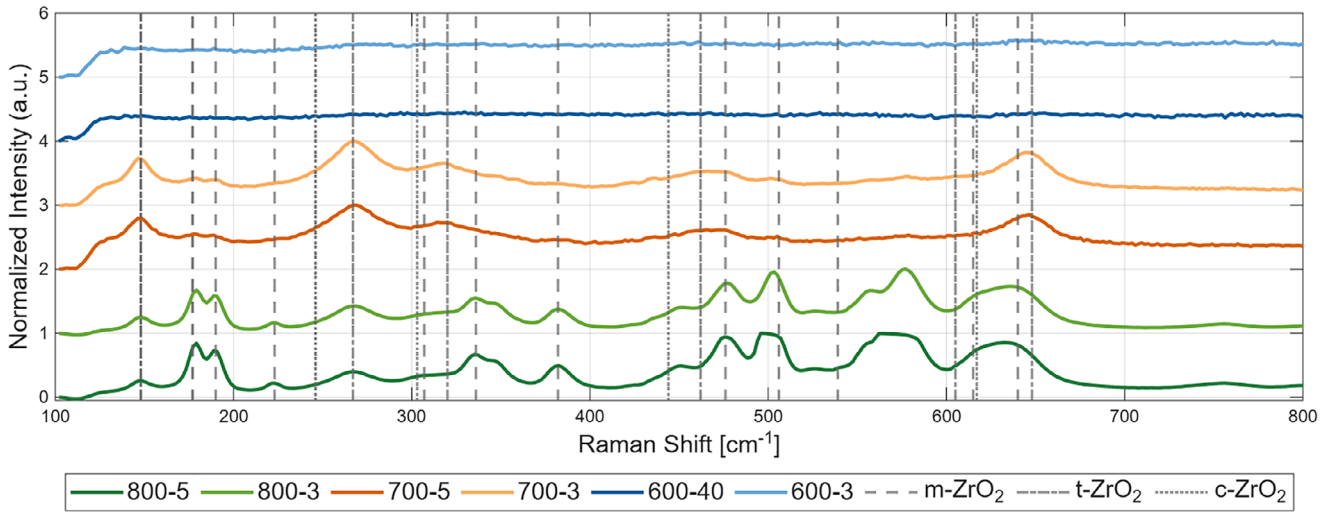


FIGURE 7 | Raman spectra of all samples after four thermal cycles from 100 to 800 cm^{-1}.

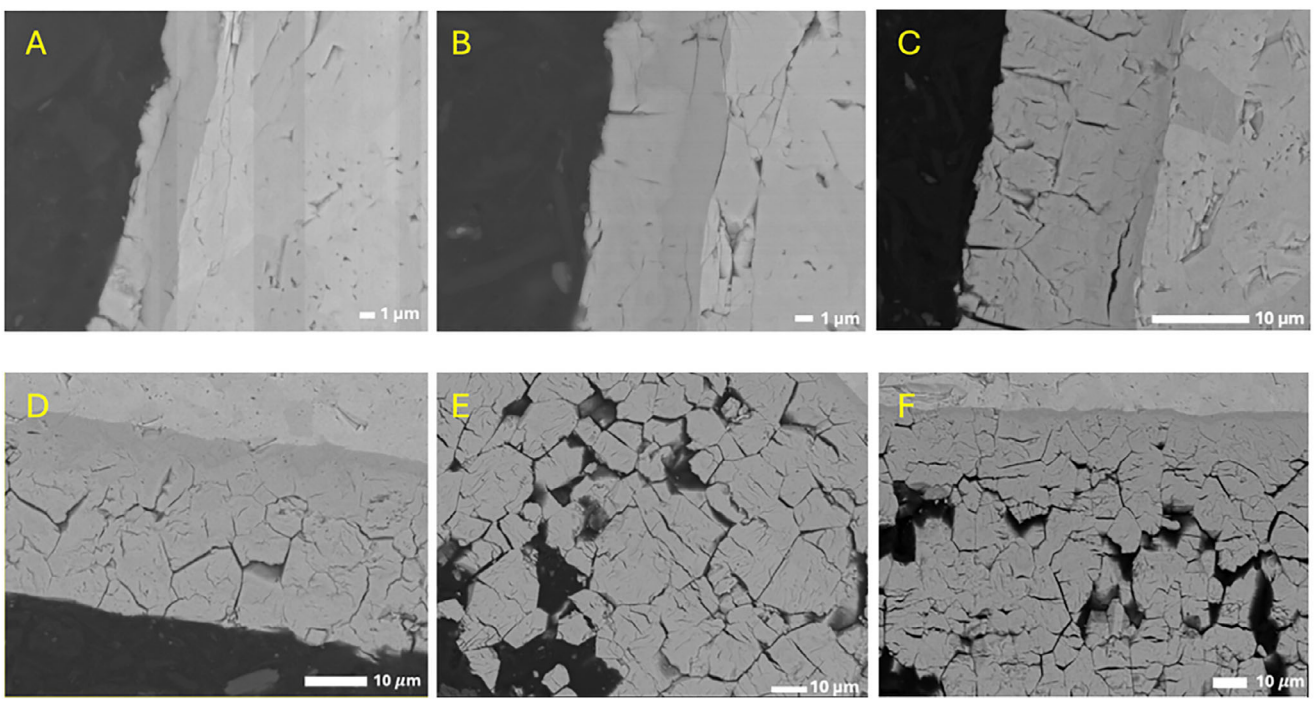


FIGURE 8 | Internal cracking of samples (A) 600-3, (B) 600-40, (C) 700-3, (D) 700-5, (E) 800-3, and (F) 800-5 after thermal cycling. Additional images of each sample after thermal cycling can be found in Figures S1–S12.

ZrO_2 transformed into the monoclinic form during rapid cooling. Although thermal shock was performed by water quenching, no evidence of new crystalline phases attributable to water exposure was detected by XRD, suggesting that the observed diffraction changes primarily reflect thermally induced $t/c \rightarrow m$ transformation.

Because this $t/c \rightarrow m$ transformation is accompanied by volumetric expansion, it introduces additional internal stress into the oxide scale [7]. Accordingly, the measured increase in monoclinic phase fraction was used as an indicator of the evolving transformation-induced stress state within the oxide scale. The Rietveld-refined phase fractions therefore provide a mechanistic basis for interpreting stress evolution during oxidation and subsequent thermal shock. The measured increase in m-ZrO_2 content further suggests that phases previously stabilized by fine grain size or mechanical constraint became unstable during rapid cooling, allowing additional transformation to occur. Consequently, samples exhibiting larger increases in monoclinic content are inferred to have experienced greater stress redistribution during quenching, as transformation strain was accommodated through crack propagation, delamination, and local stress relaxation.

17447402, 2026, 5, Downloaded from https://ceramics.onlinelibrary.wiley.com/doi/10.1111/ijac.70284 by Technical University Delft, Wiley Online Library on [01/10/2026]. See the Terms and Conditions (https://onlinelibrary.wiley.com/terms-and-conditions) on Wiley Online Library for rules of use; OA articles are governed by the applicable Creative Commons License

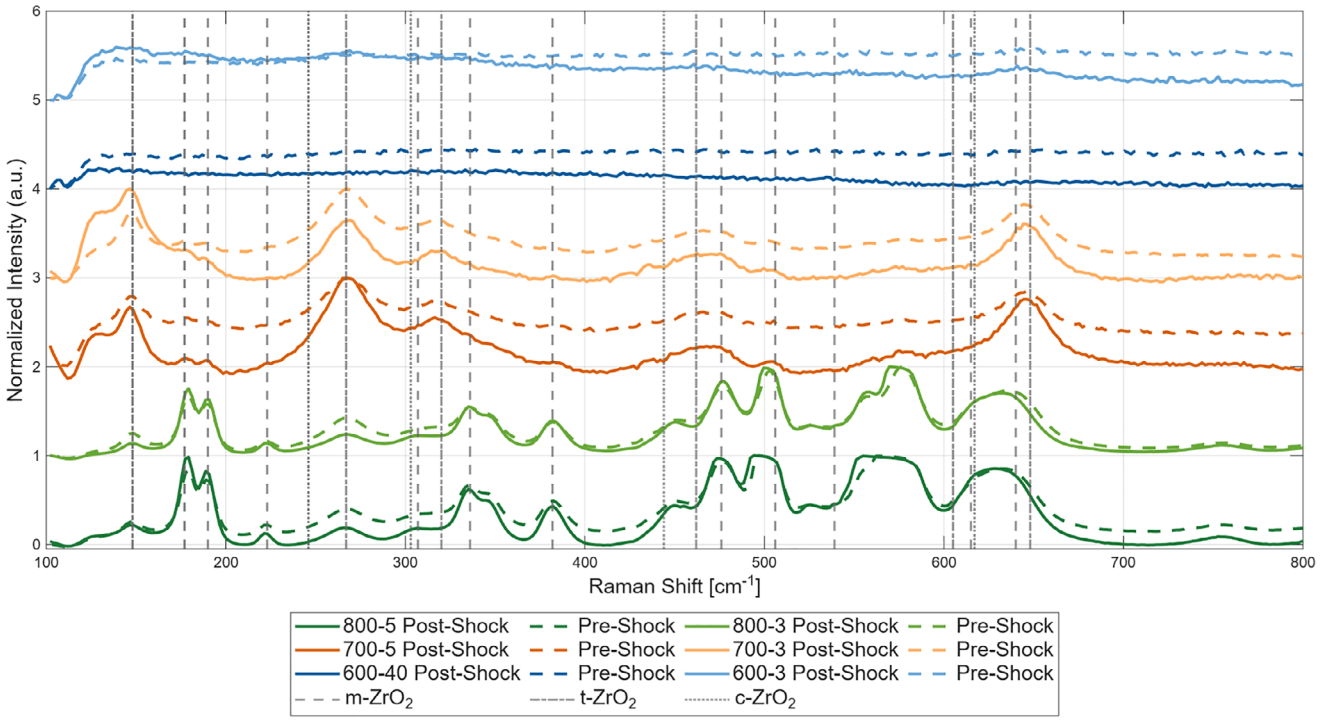


FIGURE 9 | Raman spectra of all samples before and after shock from 100 to 800 cm^{-1}.

The effect was most pronounced in samples with thicker, more cracked oxides, where pre-existing polymorphic instability was exacerbated by the shock, while heavily oxidized systems near monoclinic saturation exhibited more substantial stress-driven stabilization. In contrast, less oxidized specimens showed only minor phase redistribution.

Raman spectroscopy supported the XRD findings and provided further insight into oxide phase stability and stress evolution following thermal shock, as by the comparative pre- and post-shock spectra for all the samples (Figure 9). After quenching, the *m*-ZrO_2 peaks became more pronounced, consistent with a *t*/*c*→*m* transformation during rapid cooling. At the same time, the broad spectral feature near 1000 cm^{-1} (linked to stress or structural disorder) became more uniform, suggesting that transformation strain and surface cracking helped redistribute residual stress during thermal shock. The comparison across all oxidation conditions demonstrates that the Raman response depends strongly on the prior oxidation state. Lightly oxidized 600-series samples remained relatively feature-poor and exhibited limited evolution of distinct zirconia peaks following quenching, whereas the 700-series samples showed more pronounced changes in spectral features. The well-developed zirconia spectra of the 800-series remained comparatively consistent before and after shock, suggesting less extensive additional spectral reorganization during quenching. These qualitative spectral changes are quantified in the subsequent residual stress analysis, which relates Raman peak shifts to the evolution of local stress within the oxide following thermal shock.

To further quantify the stress evolution inferred from the Raman spectra, Raman-derived residual stress changes were calculated from shifts in the selected zirconia Raman modes (Table 4).

TABLE 4 | Changes in Raman-derived residual stress at selected peaks after thermal shock.

Sample	Monoclinic, 178 cm^{-1}	Monoclinic, 190 cm^{-1}	Tetragonal, 145 cm^{-1}
700-3	−0.2626 GPa	0.4273 GPa	0.0455 GPa
700-5	−0.1025 GPa	−0.7162 GPa	−0.5657 GPa
800-3	0.0721 GPa	−0.0029 GPa	0.1365 GPa
800-5	0.3742 GPa	0.3785 GPa	0.3854 GPa

Because the objective was to evaluate stress redistribution caused by thermal shock, only changes in residual stress pre- and post-shock are presented. Samples 600-3 and 600-40 were excluded because the limited oxide growth produced weak and poorly resolved zirconia Raman peaks, preventing reliable quantitative residual stress determination. The remaining samples exhibited relatively modest stress changes following thermal shock, generally within ±0.7 GPa. The 700-series specimens showed the greatest mode-dependent stress redistribution, with both increases and decreases in residual stress depending on the Raman mode, indicating localized redistribution between compressive and tensile stress states during quenching rather than uniform stress relaxation. In contrast, the 800-series specimens exhibited more consistent stress behavior across the analyzed modes. Sample 800-3 showed minimal changes in residual stress, suggesting that the oxide retained a relatively stable stress state during thermal shock, whereas Sample 800-5 exhibited a positive stress change of approximately 0.38 GPa for all three modes, indicating a systematic shift toward a less compressive (or more tensile) residual stress state.

17447402, 2026, 5, Downloaded from https://ceramics.onlinelibrary.wiley.com/doi/10.1111/ijac.70284 by Technical University Delft, Wiley Online Library on [01/10/2026]. See the Terms and Conditions (https://onlinelibrary.wiley.com/terms-and-conditions) on Wiley Online Library for rules of use; OA articles are governed by the applicable Creative Commons License

TABLE 5 | Crack density (surface and internal) **change** after thermal shock.

Image	600-3	600-40	700-3	700-5	800-3	800-5
Surface	2.20%	3.90%	6.51%	0.30%	0.47%	2.03%
Cross-Section	0.88%	0.32%	1.04%	1.30%	0.04%	2.20%

SEM analysis revealed that thermal shock primarily intensified surface cracking, with changes in crack density summarized in Table 5. Surface crack density increased most in moderately oxidized samples, particularly 700–3 (6.51%), where oxide layers remained intact but were vulnerable to thermal mismatch. This behavior is consistent with the Raman-derived residual stress changes (Table 4), which showed the greatest mode-dependent stress redistribution in the 700-series specimens.

Consequently, thermal shock promoted the extension and interconnection of pre-existing surface cracks, producing more continuous crack networks across the oxide surface. Although Sample 700-5 experienced a longer oxidation duration than 700-3, it exhibited a smaller increase in surface crack density (0.3%). The pre-shock outer oxide scale of 700-5 was approximately 30 μm thick compared with approximately 19 μm for 700-3. For a thin oxide scale carrying an approximately uniform residual stress, the energy release rate available to drive delamination can be approximated as

$$G \sim \frac{\sigma^2 h\,(1-\nu)}{E}$$

where σ is the residual stress, h is the oxide thickness, E is the elastic modulus, and ν is the oxide Poisson's ratio. Delamination is expected when $G = G_c$, giving an approximate critical stress of

$$\sigma_c \approx \sqrt{\frac{EG_c}{h\,(1-\nu)}}$$

where G_c is the interfacial fracture energy. Thus, increasing oxide thickness increases the energy available to drive delamination and reduces the critical stress required for interfacial failure. No experimental measurements of the interfacial fracture energy of the thermally grown ZrO_2 were identified in the literature. Atomistic studies have reported work of adhesion of approximately 0.8–1.0 eV Å^2 (≈13–16 J/m^2) for ideal crystalline ZrO_2/ZrC interfaces, providing a reference for the interfacial cohesion of the system [30]. Together with E = 217.4 GPa, ν = 0.30 for m-ZrO_2 [31], and the experimentally measured oxide-scale thickness of 29.6 μm for Sample 700-5, the idealized interfacial adhesion energy corresponds to a critical residual stress of approximately 0.37–0.41 GPa for delamination, which is within the range of the experimentally observed Raman-derived stress changes of approximately ±0.7 GPa. These values represent the reversible separation energy of an ideal crystalline interface and can therefore be regarded as an idealized upper reference for interfacial cohesion rather than a direct measure of the effective fracture energy of the thermally grown oxide scale. The effective resistance to delamination in the present specimens is expected to be lower due to microcracking, porosity, residual stress, and interface defects.

Within this framework, the greater oxide thickness of 700-5 would increase the energy available to drive delamination and reduce the critical stress required for interfacial failure relative to the thinner scale of 700-3. This provides a possible explanation for the smaller increase in surface crack density observed for 700-5 and is consistent with its greater reduction in outer oxide thickness after shock, suggesting that a greater proportion of the damage was accommodated through local delamination and oxide loss rather than additional surface cracking.

In contrast, heavily oxidized 800-series samples showed relatively low surface crack density change (2.03%), but exhibited early signs of oxide spallation, especially in Sample 800–5 (Figures 10 and 11), which also showed the highest internal crack density (2.2%), a signature of subsurface adhesive failure. The relatively consistent Raman-derived residual stress changes measured across the analyzed modes in the 800-series suggest that a substantial portion of the oxidation-induced stresses had already been accommodated during thermal cycling. In particular, the systematic shift toward a less compressive residual stress state observed for Sample 800-5 is consistent with partial stress relief through local oxide detachment. Therefore, thermal shock primarily redistributed the remaining stresses through crack widening, local delamination, and early-stage spallation rather than through extensive formation of new surface cracks.

Rather than generating large numbers of new surface cracks, thermal shock in these specimens promoted widening of existing cracks, local delamination, and oxide detachment, indicating a transition from surface fracture to interfacial failure. Despite significant oxide-scale cracking and localized spallation, cross-sectional SEM observations showed no clear evidence of additional thermal-shock-induced cracking within the underlying ZrC substrate (cross-sectional images can be seen in the Supporting Information). This behavior is consistent with the differing thermomechanical responses of the oxide and substrate; the zirconia scale has a lower tolerance for stresses induced by phase transformations and thermal mismatch compared to the underlying ZrC, allowing damage to be accommodated within the oxide before substrate fracture could occur.

These trends indicate that surface cracking dominates in less-degraded oxides, where transient thermal gradients during quenching drive damage, while more severely oxidized layers tend toward delamination and interfacial failure. This behavior is consistent with classical thermal shock theory, which predicts that crack initiation and propagation are governed by the combined effects of elastic modulus, fracture resistance, thermal expansion coefficient, and thermal conductivity. Although the mechanical properties of the thermally grown oxide scales were not measured directly, literature data for zirconia thin films provide a useful reference for assessing the stress levels associated with oxide failure. Scardi et al. investigated residual stresses in CaO-stabilized ZrO_2 thin films deposited by radio-frequency magnetron sputtering and reported compressive stresses approaching 2.8 GPa, which they identified as approximately the maximum stress sustainable by

17447402, 2026, 5, Downloaded from https://ceramics.onlinelibrary.wiley.com/doi/10.1111/ijac.70284 by Technical University Delft, Wiley Online Library on [01/10/2026]. See the Terms and Conditions (https://onlinelibrary.wiley.com/terms-and-conditions) on Wiley Online Library for rules of use; OA articles are governed by the applicable Creative Commons License

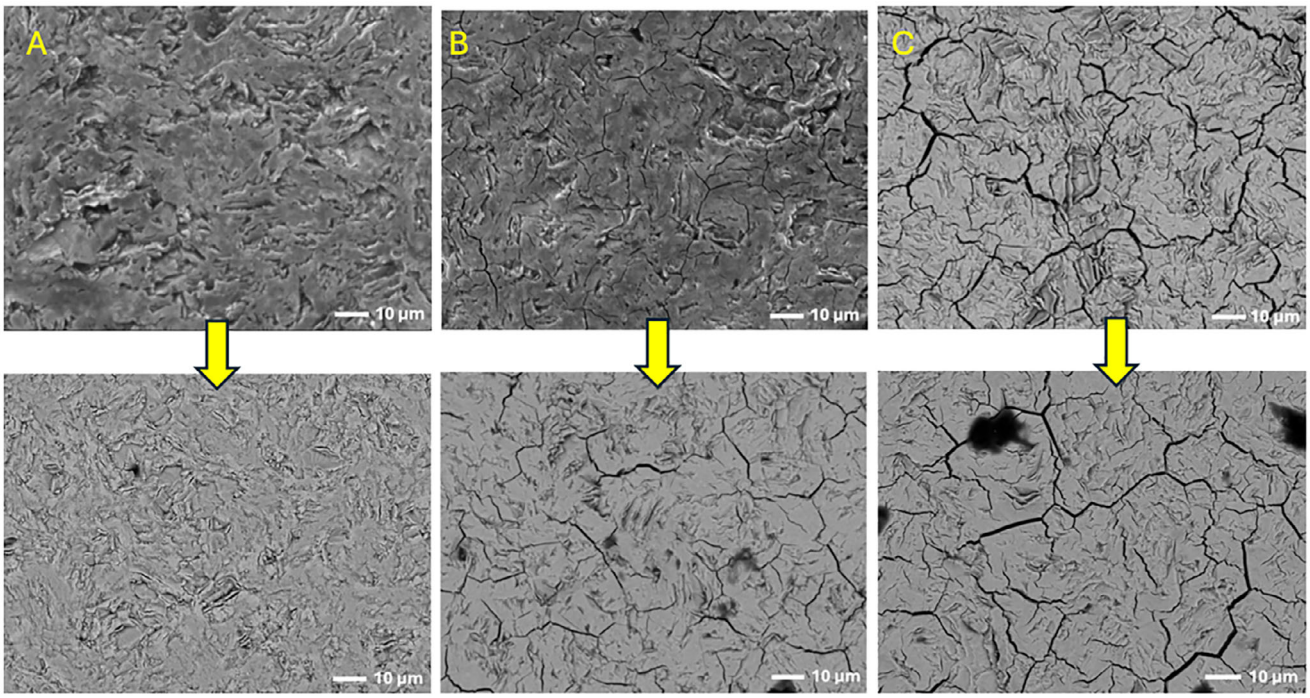


FIGURE 10 | Surface cracking of samples (A) 600-3, (B) 600-40, and (C) 700-3 before and after thermal shock. Additional images of each sample after thermal shock can be found in Figures S13–S24.

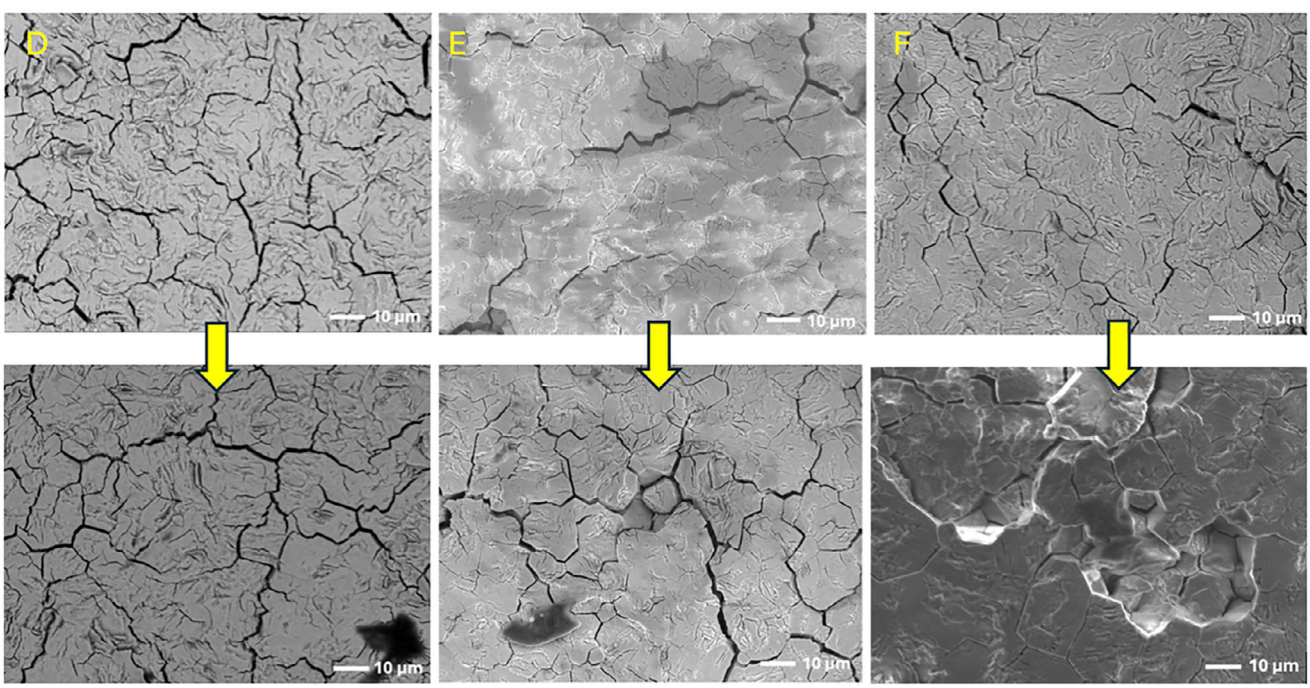


FIGURE 11 | Surface cracking of samples (D) 700-5, (E) 800-3, and (F) 800-5 before and after thermal shock. Additional images of each sample after thermal shock can be found in Figures S13–S24.

their film–substrate system [32]. In comparison, the Raman-derived stress changes measured in the present study were generally within ±0.7 GPa. These changes occurred in oxide scales that had already accumulated residual stress during oxidation, indicating that thermal shock produced substantial redistribution of an existing stress state. Together with the increased oxide thickness and observed delamination and spallation at higher oxidation severity, this comparison supports the progression toward interfacial failure observed experimentally.

17447402, 2026, 5, Downloaded from https://ceramics.onlinelibrary.wiley.com/doi/10.1111/ijac.70284 by Technical University Delft, Wiley Online Library on [01/10/2026]. See the Terms and Conditions (https://onlinelibrary.wiley.com/terms-and-conditions) on Wiley Online Library for rules of use; OA articles are governed by the applicable Creative Commons License

Unlike the moderate 20°C/min heating and cooling rates used during thermal cycling, water quenching imposes cooling rates on the order of several-hundred°C/min, generating much steeper temperature gradients and correspondingly larger transient thermal stresses. These rapidly developed stresses are concentrated near the oxide surface, making thermal shock particularly effective at promoting the propagation, widening, and interconnection of pre-existing surface cracks. This behavior is consistent with the thermal expansion mismatch between the ZrO_2 scale and ZrC substrate. Literature-cited CTE values indicate that ZrO_2 generally undergoes greater thermal strain than ZrC during cooling, while *m*-ZrO_2 exhibits additional anisotropic expansion behavior. During rapid quenching, these differences generate tensile and shear stresses within the oxide and at the oxide–substrate interface, promoting crack propagation, delamination, and eventual spallation while leaving the substrate structurally intact.

Internal crack densities, however, changed relatively little between pre- and post-shock, as evident in multi-scale SEM images provided in the Supporting Information, which show only minor qualitative changes in internal crack morphology. Although XRD and Raman measurements probe only the surface, the observed stability of internal cracks suggests that subsurface damage is primarily governed by cyclic oxidation-induced stresses (such as CTE mismatch and phase transformation strain) accumulated during oxide growth, rather than by transient thermal shock. While the exact phase composition deeper inside the oxide cannot be directly measured in this study, the limited change in internal cracking indicates that these oxidation-driven stresses dominate the subsurface, whereas surface cracking remains the most sensitive indicator of additional thermal shock damage.

These observations highlight that thermal shock exacerbates pre-existing oxidation damage differently depending on oxide maturity: thinner, less-cracked oxides accumulate additional surface cracking, while thicker, more extensively transformed scales increasingly exhibit delamination and spallation. The previously discussed stress limits reported for stabilized ZrO_2 films provide useful context for the magnitude of stresses that can promote mechanical accommodation in zirconia scales [30]. In the present study, thermal-shock-induced Raman-derived stress changes were generally within ±0.7 GPa and occurred in oxide scales that had already accumulated oxidation-induced residual stress, cracking, and phase-transformation strain during thermal cycling. Thus, the measured stress redistribution, together with increasing oxide thickness and pre-existing damage, is consistent with the progression toward delamination and spallation observed in the more heavily oxidized samples.

Overall, these results confirm that thermal shock induces measurable structural and mechanical changes in oxidized ZrC. Phase analysis revealed continued $t/c \rightarrow m$ transformation during shock, while Raman and SEM data showed evidence of stress redistribution, surface cracking, and, in the most degraded samples, early-stage spallation. The severity of these effects scaled with prior oxidation temperature and monoclinic content, highlighting oxidation history as a key factor controlling post-shock damage evolution.

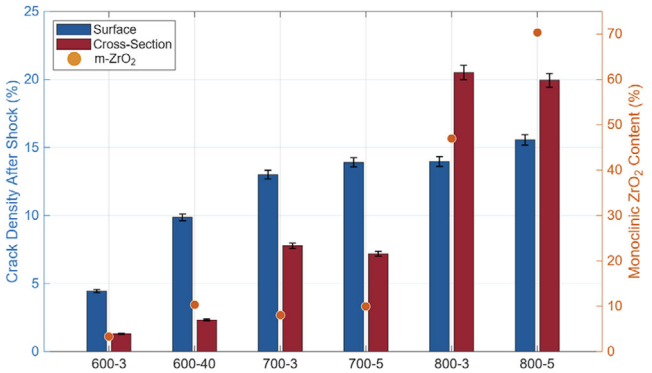


FIGURE 12 | Comparison of post-shock *m*-ZrO_2 content with surface and internal crack densities.

3.4 | Degradation Threshold Identification

To evaluate the influence of oxidation history on thermal shock resistance, degradation thresholds were introduced to identify the transition from stable oxide growth to severe mechanical degradation. Because no universally accepted degradation criterion exists for oxidized ZrC subjected to coupled oxidation and thermal shock, the thresholds identified in this study are intended as practical screening criteria rather than universal failure limits. They provide a consistent framework for comparing oxidation conditions and identifying the onset of structural instability.

The selection of these thresholds was guided by observations from related ceramic systems. In thermal barrier coatings, NASA defines failure when oxide spallation covers approximately 10% of the coating surface, indicating the loss of protective function [33]. Similarly, zirconia ceramics exhibiting approximately 10% crack density have been reported to undergo saturation of transformation-induced plasticity accompanied by an approximately 30% reduction in Young's modulus, indicating a significant loss of stiffness and strain accommodation capability [34].

Likewise, studies of biomedical zirconia show that once monoclinic content approaches 20%, surface roughness increases dramatically and microcrack networks become apparent, while additively manufactured zirconia exhibits approximately a 21% reduction in flexural strength as monoclinic content increases from approximately 7% to approximately 9% [35, 36]. Collectively, these studies indicate that degradation in zirconia-containing ceramics often accelerates once monoclinic content or crack density reaches approximately 10%. This range therefore provides a practically meaningful basis for identifying the onset of instability. Accordingly, a value of 10% was adopted in this study as a screening threshold for both monoclinic content and post-shock surface crack density.

These trends are illustrated in the composite plot of pre-shock monoclinic content and pre- and post-shock crack density (Figure 12). While the 700°C samples hovered near the proposed failure thresholds (10% surface crack density or monoclinic content), the 800°C series exceeded both criteria. These samples displayed the most severe damage types, including oxide delam-

17447402, 2026, 5, Downloaded from https://ceramics.onlinelibrary.wiley.com/doi/10.1111/ijac.70284 by Technical University Delft, Wiley Online Library on [01/10/2026]. See the Terms and Conditions (https://onlinelibrary.wiley.com/terms-and-conditions) on Wiley Online Library for rules of use; OA articles are governed by the applicable Creative Commons License

ination and internal voiding, representing a shift from surface-limited degradation to structural failure. These behaviors were further exacerbated by thermal expansion mismatch between the oxide and ZrC substrate. The anisotropic expansion of *m*-ZrO_2 likely promoted interfacial stress and delamination during rapid cooling. Supporting this, the narrowing of the 1000 cm^{-1} Raman band after shock suggests that residual stress was relieved through cracking or oxide detachment.

Based on the obtained data, it becomes clear that the oxidation history of ZrC plays a decisive role in governing post-shock damage evolution. The thermal shock response of oxidized monolithic ZrC was governed by the phase composition and structural condition of the pre-existing oxide layer. As shown in Figure 12, oxides with high *m*-ZrO_2 content were especially prone to cracking, delamination, and spallation, consistent with degradation mechanisms driven by polymorphic instability and thermal expansion mismatch.

One notable observation is that surface crack density appeared to plateau at the highest oxidation temperatures, whereas internal crack density increased more rapidly. This suggests a shift in the dominant damage mechanism with increasing oxidation severity. In thinner oxides, thermal shock stresses are primarily accommodated through the formation of new surface cracks. As oxidation progresses and the oxide thickens, damage increasingly manifests as internal crack propagation, interfacial delamination, and spallation driven by accumulated oxidation-induced stresses. Consequently, additional oxidation does not necessarily increase the number of observable surface cracks, explaining the apparent plateau in surface crack density despite continued growth in internal damage.

Importantly, these thresholds are supported by experimental observations. Samples oxidized at 700°C remained close to, but generally below, the proposed limits and exhibited predominantly surface-localized cracking. In contrast, the 800°C specimens exceeded both thresholds and consistently showed delamination, internal voiding, and early-stage spallation. Thus, the proposed thresholds serve as practical reference points for identifying the experimentally observed transition in damage mechanisms within the conditions investigated in this study. The agreement between the proposed criteria and the observed transition in damage mechanisms suggests that the selected thresholds provide a meaningful indicator of the onset of structural instability for the oxidation and thermal shock conditions investigated in this study.

4 | Conclusions

This study systematically investigated the influence of cyclic oxidation on the thermal shock response of monolithic ZrC. Thermal cycling in the 600–800°C range induced a progressive evolution of the oxide scale, with low-temperature oxidation producing metastable *t*/*c*-ZrO_2 and higher temperature exposure promoting the formation of monoclinic ZrO_2. This phase transformation, accompanied by residual stress accumulation and increased crack density, established a spectrum of oxide surface states ranging from compliant, thin layers to thick, brittle scales. The measured evolution from *t*/*c*-ZrO_2 to *m*-ZrO_2 further indicated progressive stress development within the oxide scale, driven by transformation-induced strain and thermal expansion mismatch with the ZrC substrate.

Subsequent thermal shock testing revealed that the mechanical response of ZrC strongly depends on the pre-existing oxide condition. Lightly oxidized samples primarily developed additional surface cracks, whereas heavily oxidized, monoclinic-rich oxides exhibited spallation and delamination. Raman-derived residual stress analysis indicated that thermal shock altered the existing oxidation-induced residual stress distribution, with the extent of stress redistribution depending on oxide maturity. Internal cracking was largely determined by oxidation history rather than transient shock loads, indicating that the severity of pre-shock oxide evolution governs the dominant failure mode under rapid cooling. The observed damage remained confined to the oxide scale, consistent with thermomechanical stresses being concentrated within the oxide and near the oxide–substrate interface, while the ZrC substrate retained its structural integrity under the conditions investigated in this study. More severe thermal shock conditions may eventually exceed the mechanical limits of the substrate, and further investigation at larger temperature gradients would be needed to establish the transition from oxide-scale failure to substrate damage.

By correlating phase composition, stress indicators, and crack density, this work identified degradation thresholds for ZrC under coupled oxidative and thermal shock conditions. Samples oxidized at 800°C exceeded both 10% monoclinic content and 10% surface crack density, marking the onset of structural instability and adhesive oxide failure. The proposed thresholds provide practical reference points for identifying the experimentally observed transition from surface cracking to interfacial degradation under the conditions examined in this study, rather than universal failure limits for all ZrC applications. These findings highlight the critical role of oxidation history in controlling thermal shock resilience. While the maximum temperature in thermal shock was limited to the same temperature as in thermal cycling in this study, it can be inferred that more severe thermal shock conditions will likely exceed the degradation threshold, and the findings in this work could provide practical guidance for the safe use of ZrC in high-temperature cyclic environments.

Overall, this study links oxidation-driven surface evolution to post-shock failure by relating phase evolution, residual stress development, and the thermomechanical response of the oxide/substrate system. More broadly, the results provide a transferable framework for defining degradation thresholds in UHTCs and evaluating thermal shock resilience across related systems.

Author Contributions

Eden Pfanner: conceptualization, methodology, validation, investigation, formal analysis, Writing – original draft, visualization. **Yun-Ching Lin:** conceptualization, resources, writing – review and editing, supervision. **Yinglu Tang:** conceptualization, validation, writing – review and editing, supervision, funding acquisition.

17447402, 2026, 5, Downloaded from https://ceramics.onlinelibrary.wiley.com/doi/10.1111/ijac.70284 by Technical University Delft, Wiley Online Library on [01/10/2026]. See the Terms and Conditions (https://onlinelibrary.wiley.com/terms-and-conditions) on Wiley Online Library for rules of use; OA articles are governed by the applicable Creative Commons License

Acknowledgments

We would like to acknowledge the Department of Aerospace Structures and Materials at the Faculty of Aerospace Engineering in TU Delft for funding this research. We would also like to thank Roy Awater and Hans Brouwer for technical support during the performance of material characterization.

Conflicts of Interest

The authors declare no conflicts of interest.

Data Availability Statement

The data that support the findings of this study are openly available in TU Delft Repository at https://resolver.tudelft.nl/uuid:09966fef-d524-481a-bdb4-a74621a5a66a

References

1. G. Peterson, R. Carr, and E. Marinero, "Zirconium Carbide for Hypersonic Applications, Opportunities and Challenges," *Materials* 16 (2023): 6158, https://doi.org/10.3390/ma16186158.

2. S. Meng, G. Liu, Y. Guo, X. Xu, and F. Song, "Mechanisms of Thermal Shock Failure for Ultra-High Temperature Ceramic," *Materials and Design* 30 (2009): 2108–2112.

3. C. Gasparrini, R. J. Chater, D. Horlait, L. Vandeperre, and W. E. Lee, "Zirconium Carbide Oxidation: Kinetics and Oxygen Diffusion Through the Intermediate Layer," *Journal of the American Ceramic Society* 101 (2018): 2638–2652, https://doi.org/10.1111/jace.15479.

4. A. K. Kuriakose and J. L. Margrave, "The Oxidation Kinetics of Zirconium Diboride and Zirconium Carbide at High Temperatures," *Journal of the Electrochemical Society* 111 (1964): 827, https://doi.org/10.1149/1.2426263.

5. G. A. R. Rao and V. Venugopal, "Kinetics and Mechanism of the Oxidation of ZrC," *Journal of Alloys and Compounds* 206 (1994): 237–242, https://doi.org/10.1016/0925-8388(94)90042-6.

6. A. H. Ouensanga and M. Dode, "Etude Thermodynamique Et Structurale a Haute Temperature Du Systeme Zr-C-O. Diagramme De Phases a 1555°C," *Journal of Nuclear Materials* 59 (1976): 49–60, https://doi.org/10.1016/0022-3115(76)90007-6.

7. F. Frank, M. Tkadletz, C. Saringer, et al., "In-Situ Investigation of the Oxidation Behaviour of Chemical Vapour Deposited Zr(C,N) Hard Coatings Using Synchrotron X-Ray Diffraction," *Coatings* 11 (2021): 264, https://doi.org/10.3390/coatings11030264.

8. S. Shimada and T. Ishil, "Oxidation Kinetics of Zirconium Carbide at Relatively Low Temperatures," *Journal of the American Ceramic Society* 73 (1990): 2804–2808, https://doi.org/10.1111/j.1151-2916.1990.tb06678.x.

9. D. Z. Chaney, J. Hirtz, E. Williams, et al., "Grain Size Dependence of Thermally Induced Oxidation in Zirconium Carbide," *Journal of Materials Science* 58 (2023): 2439–2455, https://doi.org/10.1007/s10853-023-08145-8.

10. R. P. Haggerty, P. Sarin, Z. D. Apostolov, P. E. Driemeyer, and W. M. Kriven, "Thermal Expansion of HfO_2 and ZrO_2," *Journal of the American Ceramic Society* 97 (2014): 2213–2222, https://doi.org/10.1111/jace.12975.

11. O. J. Whittemore and N. N. Ault, "Thermal Expansion of Various Ceramic Materials to 1500°C," *Journal of the American Ceramic Society* 39 (1956): 443–444, https://doi.org/10.1111/j.1151-2916.1956.tb15619.x.

12. K. M. Doleker, Y. Ozgurluk, H. Ahlatci, and A. C. Karaoglanli, "Evaluation of Oxidation and Thermal Cyclic Behavior of YSZ, $Gd_2Zr_2O_7$ and YSZ/$Gd_2Zr_2O_7$ TBCs," *Surface & Coatings Technology* 371 (2019): 262–275, https://doi.org/10.1016/j.surfcoat.2018.11.055.

13. D. Hasselman, "Unified Theory of Thermal Shock Fracture Initiation and Crack Propagation in Brittle Ceramics," *Journal of the American Ceramic Society* 52 (1969): 600–604, https://doi.org/10.1111/j.1151-2916.1969.tb15848.x.

14. T. J. Lu and N. A. Fleck, "The Thermal Shock Resistance of Solids," *Acta Metallurgica* 46 (1998): 4755–4768, https://doi.org/10.1016/S1359-6454(98)00127-X.

15. S. E. Landwehr, G. E. Hilmas, W. G. Fahrenholtz, I. G. Talmy, and H. Wang, "Thermal Properties and Thermal Shock Resistance of Liquid Phase Sintered ZrC–Mo Cermets," *Materials Chemistry and Physics* 115 (2009): 690–695, https://doi.org/10.1016/j.matchemphys.2009.02.012.

16. S. Meng, G. Liu, Y. Guo, X. Xu, and F. Song, "Mechanisms of Thermal Shock Failure for Ultra-High Temperature Ceramic," *Materials and Design* 30 (2009): 2108–2112, https://doi.org/10.1016/j.matdes.2008.08.031.

17. L. Chen, A. Wang, X. Suo, P. Hu, X. Zhang, and Z. Zhang, "Effect of Surface Heat Transfer Coefficient Gradient on Thermal Shock Failure of Ceramic Materials Under Rapid Cooling Condition," *Ceramics International* 44 (2018): 8992–8999, https://doi.org/10.1016/j.ceramint.2018.02.100.

18. L. Zhang, Z. Tong, R. He, et al., "Key Issues of $MoSi_2$-UHTC Ceramics for Ultra High Temperature Heating Element Applications: Mechanical, Electrical, Oxidation and Thermal Shock Behaviors," *Journal of Alloys and Compounds* 780 (2019): 156–163, https://doi.org/10.1016/j.jallcom.2018.11.384.

19. M. T. Konnik, T. Oldham, A. Rzepka, V. Le Maout, K. A. Stephani, and F. Panerai, "High-Temperature Oxidation and Nitridation of Substoichiometric Zirconium Carbide in Isothermal Air," *Journal of the European Ceramic Society* 44 (2024): 6771–6776, https://doi.org/10.1016/j.jeurceramsoc.2024.04.006.

20. E. Courtright, J. Prater, G. Holcomb, G. Pierre, and R. Rapp, "Oxidation of Hafnium Carbide and Hafnium Carbide With Additions of Tantalum and Praseodymium," *Oxidation of Metals* 36 (1991): 423–437, https://doi.org/10.1007/BF01151590.

21. S. R. Levine, E. J. Opila, M. C. Halbig, J. D. Kiser, M. Singh, and J. A. Salem, "Evaluation of Ultra-High Temperature Ceramics for Aeropropulsion Use," *Journal of the European Ceramic Society* 22 (2002): 2757–2767, https://doi.org/10.1016/S0955-2219(02)00140-1.

22. Y. Lin, H. Brouwer, V. Popovich, and Y. Tang, "Three-Stage Oxidation Kinetics and Passivation Mechanism of Spark Plasma Sintered ZrC Ultra-High Temperature Ceramic," *Journal of the European Ceramic Society* 46 (2026): 117757, https://doi.org/10.1016/j.jeurceramsoc.2025.117757.

23. S. I. Moseenkov, V. L. Kuznetsov, N. A. Zolotarev, et al., "Investigation of Amorphous Carbon in Nanostructured Carbon Materials: A Comparative Study by TEM, XPS, Raman Spectroscopy and XRD," *Materials* 16 (2023): 1112, https://doi.org/10.3390/ma16031112.

24. K. Suchorab, M. Gawęda, and L. Kurpaska, "Comparison of Raman Imaging Assessment Methods in Phase Determination and Stress Analysis of Zirconium Oxide Layer," *Spectrochimica Acta Part A: Molecular and Biomolecular Spectroscopy* 295 (2023): 122625.

25. G. Pezzotti and A. Porporati, "Raman Spectroscopic Analysis of Phase-Transformation and Stress Patterns in Zirconia Hip Joints," *Journal of Biomedical Optics* 9 (2004): 372–384, https://doi.org/10.1117/1.1647547.

26. L. Kurpaska, M. Lesniak, R. Jadach, M. Sitarz, J. Jasinski, and J. Grosseau-Poussard, "Shift in Low-Frequency Vibrational Spectra Measured In-Situ at 600°C by Raman Spectroscopy of Zirconia Developed on Pure Zirconium and Zr–1%Nb Alloy," *Journal of Molecular Structure* 1126 (2016): 186–191, https://doi.org/10.1016/j.molstruc.2016.03.001.

27. A. Bumajdad, A. A. Nazeer, F. Al Sagheer, S. Nahar, and M. I. Zaki, "Controlled Synthesis of ZrO_2 Nanoparticles With Tailored Size, Morphology and Crystal Phases via Organic/Inorganic Hybrid Films," *Scientific Reports* 8 (2018): 3695, https://doi.org/10.1038/s41598-018-22088-0.

28. S. Ding, J. Zhao, and Q. Yu, "Effect of Zirconia Polymorph on Vapor-Phase Ketonization of Propionic Acid," *Catalysts* 9 (2019): 768, https://doi.org/10.3390/catal9090768.

29. D. Tuschel, "Exploring Resonance Raman Spectroscopy," *Spectroscopy* 33 (2018): 12–19.

17447402, 2026, 5, Downloaded from https://ceramics.onlinelibrary.wiley.com/doi/10.1111/ijac.70284 by Technical University Delft, Wiley Online Library on [01/10/2026]. See the Terms and Conditions (https://onlinelibrary.wiley.com/terms-and-conditions) on Wiley Online Library for rules of use; OA articles are governed by the applicable Creative Commons License

30. E. Osei-Agyemang, J. Paul, R. Lucas, et al., "Characterizing the ZrC(111)/c-ZrO_2(111) Hetero-Ceramic Interface: First Principles DFT and Atomistic Thermodynamic Modeling," *Molecules* 27, no. 9 (2022): 2954, https://doi.org/10.3390/molecules27092954.

31. K. Balakrishnan, V. Veerapandy, V. Nalini, and P. Vajeeston, "Density Functional Theory Analysis of Novel ZrO_2 Polymorphs: Unveiling Structural Stability, Electronic Structure, Vibrational and Optical Properties," *Computational Materials Science* 246 (2025): 113439, https://doi.org/10.1016/j.commatsci.2024.113439.

32. P. Scardi, P. Polonioli, and S. Ferrari, "Residual Stress in Stabilized Zirconia Thin Films Prepared by R.f. Magnetron Sputtering," *Thin Solid Films* 253 (1994): 349–355, https://doi.org/10.1016/0040-6090(94)90346-8.

33. R. V. Hillery, B. H. Pilsner, and E. C. Duderstadt, "Thermal Barrier Coating Life Prediction Model Development," NASA N88-11184, NASA Lewis Research Center; General Electric Aircraft Engine Business Group, 1988.

34. P. E. Reyes-Morel and I. Chen, "Stress-Biased Anisotropic Microcracking in Zirconia Polycrystals," *Journal of the American Ceramic Society* 73 (1990): 1026–1033.

35. L. Yoo, N. Pang, S. Kim, and B. Jung, "Mechanical Properties of Additively Manufactured Zirconia With Alumina Air Abrasion Surface Treatment," *Scientific Reports* 13 (2023): 9153, https://doi.org/10.1038/s41598-023-36181-6.

36. J. Chevalier, L. Gremillard, and S. Deville, "Low-Temperature Degradation of Zirconia and Implications for Biomedical Implants," *Annual Review of Materials Research* 37 (2007): 1–32, https://doi.org/10.1146/annurev.matsci.37.052506.084250.

Supporting Information

Additional supporting information can be found online in the Supporting Information section.

Supporting File: ijac70284-sup-0001-DataS1.docx.

17447402, 2026, 5, Downloaded from https://ceramics.onlinelibrary.wiley.com/doi/10.1111/ijac.70284 by Technical University Delft, Wiley Online Library on [01/10/2026]. See the Terms and Conditions (https://onlinelibrary.wiley.com/terms-and-conditions) on Wiley Online Library for rules of use; OA articles are governed by the applicable Creative Commons License